Determination of Optimal Geometry for an Empty Concentrator Augmented Wind Turbine

.

ABSTRACT

Aims: To determine the optimal concentrator geometrical parameters of an empty concentrator augmented wind turbine (CAWT), which are used to design and install CAWTs.
Place and Duration of Study: Physics Department, University of Fort Hare, South Africa between March 2023, and October 2023.
Methodology: The study used the concentrator length (L) to concentrator outlet diameter ratio (L_r) and the difference between inlet and outlet radii to concentrator outlet diameter ratio (R_r) to investigate the effect of concentrator geometry on wind velocity augmentation and air dynamics to determine the optimum concentrator geometrical parameters using computational fluid dynamics modelling. The modelled concentrators' geometry was created in SolidWorks, prepared for meshing in SpaceClaim, meshed, and analysed in Fluent to solve the Reynolds-averaged Navier-Stokes equations, and validated by primary experimental results. To make the concentrators, six equally spaced L_r were used in the range $0.1 \leq L_r \leq 0.6$ and thirteen equally spaced R_r in the range $0.025 \leq R_r \leq 0.325$. The concentrators' performance was investigated in terms of velocity augmentation ratio (v_r) and concentrator efficiency (η_c).
Results: It was observed that the variation in v_r was influenced by the change in both L_r and R_r. The v_r and η_c increased with an increase in L_r to a maximum at optimum L_r and decreased thereafter. The optimum v_r was obtained at $L_r = 0.4$ and $R_r = 0.1$ with a maximum velocity at the concentrator outlet. It was also shown that the energy losses due to friction negatively impact velocity augmentation more than energy losses due to a large concentrator tilt angle at high L_r.
Conclusion: When constructing a CAWT, the turbine rotor should be placed at any distance between the concentrator outlet and $0.5L$ behind the concentrator, and the blade tips of the turbine in a CAWT system should be at least 10% smaller than the concentrator outlet radius, for the whole rotor to receive wind with augmented velocity.

Keywords: air dynamics; concentrator augmented wind turbine; velocity augmentation ratio; concentrator efficiency; CFD analysis; wind energy.

1. INTRODUCTION

"It is anticipated that renewable energy (RE) will be capable of supplying two-thirds of the global energy demand by 2050" [1]. "Wind energy is one of the fastest-growing, most cost-effective, clean, and least land-consuming RE resources and is expected to contribute approximately 15% to 18% of global electricity consumption" [1,2]. "However, wind has a very low energy density, implying that a more extensive rotor area or higher hub height is required to harness kinetic energy to generate meaningful electrical power" [3,4]. "This results in higher costs of producing energy from wind than conventional energy sources such as fossil fuels and hydro. Researchers have devised several initiatives to boost wind turbine power output to lower the cost of wind energy. Several mechanisms, which can be used individually or in combination, have been proposed to increase the turbine power output per unit rotor area. These include the mass concentration and energy augmentation effects on the wind" [5].

Table 1 shows the wind speed criterion for selecting wind power generation sites using turbines currently on the market. Shambira et al. (2021) indicated that most parts of the world experience low wind speeds of around 4 ms^{-1} and less for almost 330 days per year [2]. "Therefore, these areas cannot utilize wind energy for electricity generation. Several

mechanisms, such as diffuser-augmented wind turbine (DAWT), concentrator-augmented wind turbine (CAWT) system and framed light shell diffuser result in increased mass flow through the turbine so that the velocity of air reaching the turbine is greater than what it should have been if the turbine had been bare" [1,2,6,7]. "The concept of diffusers and concentrators that increase the speed of wind reaching the turbine rotor has been on the research agenda for decades, with the first in-depth study around the mid-20th century, but to date, there have been no successful commercial designs" [8]. "The motivation behind continued studies is that an insignificant rise in wind speed due to the inclusion of ducts in conventional turbine systems can cause a huge increase in power output since wind turbine power output is proportional to the cube of the wind speed [2,9]. Much research effort on ducted turbines has focused on DAWTs" [5,10,11]. A detailed review of ducted turbines has shown that 16% enhancement in the power coefficient can be achieved thus exceeding the Betz limit [12].

Table 1. **Site suitability for electricity generation at different speeds**

Average wind velocity (m/s)	Suitability for electricity generation
4	Insufficient
5	Low
6	Moderate
7	Sufficient
8	Very good

Source: [1]

"The CAWT concept involves using a funnel-shaped duct to capture wind from a larger area and deliver it to the rotor through a smaller area, thus increasing the mass flow rate. Several studies have been done on using concentrators on vertical axis wind turbines, proving that a power augmentation factor of about 3.7 can be achieved" [13]. Various names have been used for CAWTs such as nozzle augmented wind turbine which has proved to increase wind velocity while decreasing the pressure along the nozzle [14]. Limited studies involve the use of concentrators on horizontal axis wind turbines (HAWTs).

A detailed review of work that has been done to increase wind speed using CAWTs is given by Shonhiwa and Makaka [15]. They concluded that CAWTs can increase the power output in areas of low wind speed if the functionality knowledge gap is closed. The identified gaps included the absence of information about the system's operational mechanism and the influence of concentrator geometrical parameters on the performance of the concentrator.

Thangavelu et al. proposed a new CAWT design, optimized the concentrator design parameters and investigated the effect of air pressure and wind speed on the proposed CAWT design using computational fluid dynamics (CFD) simulation in Ansys Fluent [16]. Their geometry was designed using SolidWorks software with different parameters. Their major finding was that the CAWT with a nozzle angle of 20^{o} resulted in a 537% velocity increment.

Mohanan et al. (2021) simulated the performance of concentrators and diffusers in open Ansys Fluent [1]. They used concentrators with a concentrator length to outlet diameter ratio (L_r) above 1. For such long concentrators, the optimum velocity augmentation of 9.8% was achieved at $L_r \approx 1.7$. From the simulation results, they developed equations for calculating the velocity augmentation ratio in terms of the concentrator tilt (divergence) angle. They installed a CAWT using a fabricated concentrator and a purchased 100 W, 24 V direct current generator to validate the simulation results. The maximum power augmentation of 12.3% was achieved at $L_r = 1.6$. Hence, from their analysis, long concentrators are unsuitable for wind velocity and power augmentation.

The study by Mohanan et al. also noted that increasing the wall length of conical sections reduces the area swept by the rotor for a given tilt angle. Nevertheless, no studies have focused on short concentrators to find out their effect on wind augmentation. To assess the effect of short to medium concentrators on wind velocity augmentation, this study focused on analyzing the performance of concentrators with $L_r \leq$ and determined the optimal geometrical parameters of an empty concentrator. These parameters are important when designing and installing a CAWT system, which generates meaningful electricity in low wind speed areas.

2. MATERIAL AND METHODS

2.1 Computational analysis

CFD modelling was used to optimise the concentrator geometry parameters in ANSYS 2023 R1 to reduce the cost and time of experimental work. The concentrator geometry shown in Figure 1 was created in SolidWorks ® Student Edition 2023 SP2.1.

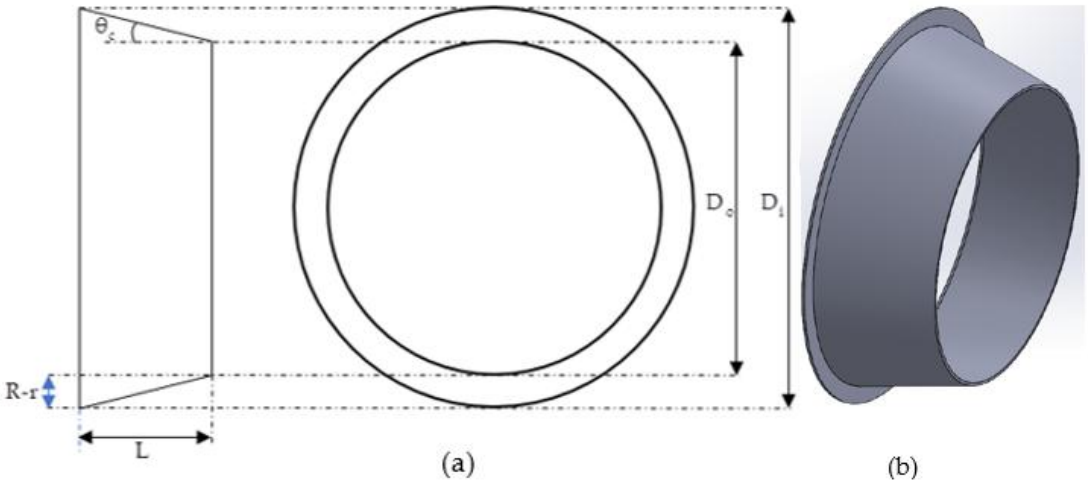

Fig 1. The concentrator geometry. (a) The geometry parameters and (b) the concentrator

The concentrator was prepared for meshing in SpaceClaim 2023 R1 and enclosed in a cylindrical virtual wind tunnel as shown in Figure 2 (a). For the CFD data to be validated with corresponding experimental data, the model interprets exactly the geometry of the concentrator. To avoid blockage effects, the tunnel was 15 concentrator outlet diameters long and 10 concentrator outlet diameters wide. Due to the symmetry of the computational domain and to save on computational time and cost, the flow domain was divided into 90° slices using the split body as shown in Figure 2 (b).

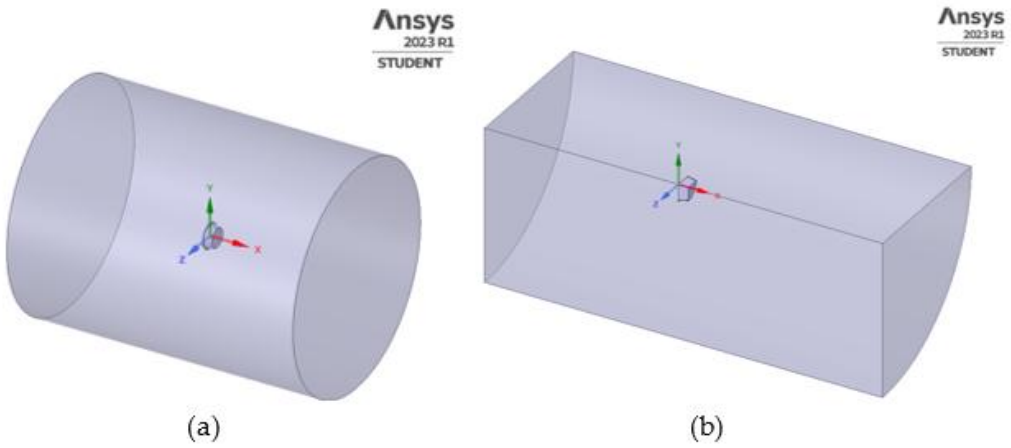

Figure 2. The concentrator in a virtual wind tunnel. (a) Entire computational flow domain and (b) one-quarter slice of the entire flow domain

The Watertight geometry workflow was followed in meshing the computational domain. Local sizing was applied to the concentrator surface and the virtual wind tunnel body. The curvature and proximity size functions were applied to generate the surface mesh shown in Figure 3 (a). 156570 faces were created with an excellent average skewness of 0.1 and a maximum skewness of 0.47. Polyhedral cells were used to volume mesh the whole domain to produce the mesh clipped in the x-direction shown in Figure 3 (b). 427713 cells were created with an excellent average orthogonal quality of

0.96662 and a maximum of 0.99998. A mesh independence test was carried out to confirm the solutions' accuracy. An average percentage relative error of 0.0017 was considered negligible.

Numerical analysis of the concentrator was conducted using ANSYS Fluent software to solve the Reynolds-averaged Navier-Stokes (RANS) equations. This study employed the k-ω turbulence model due to its effectiveness in accounting for flows near walls and providing improved predictions for near-wake flow analysis. It also addresses closure problems in RANS equations compared to standard k-ε variants, making it suitable for analyzing flows around curved surfaces, especially those with strong curvature and adverse pressure gradients. Moreover, it offers more accurate predictions for flow separation and reattachment, making it well-suited for no-slip wall conditions. The model's absence of damping functions allows for fixed boundary conditions and accurate forecasts of mean flow profiles and wall skin functions [17]. The k-ω standard turbulence model was used to simulate the flow fields within the domain, and the residual convergence criteria were set to 10^{-6}.

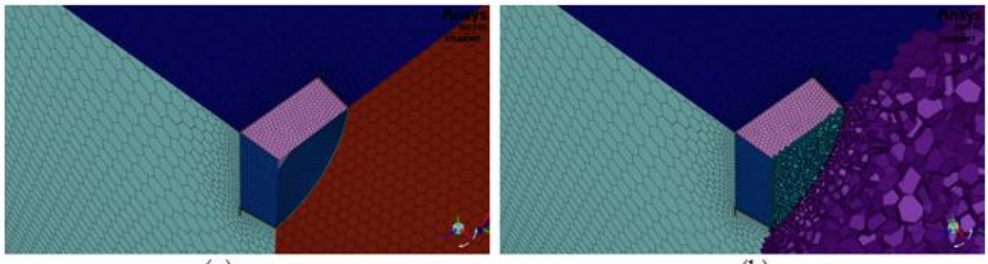

Figure 3. The meshed computational domain clipped along the x-axis. (a) Surface mash and (b) full-volume mesh

In the present problem, the flow was assumed to be incompressible, and steady, with air considered the working fluid. The primary governing equations include the conservation of mass, often called the continuity equation, and the conservation of momentum equation. Given these considerations, the differential equations for mass and momentum conservation can be expressed as follows:

Continuity equation

$$\frac{\partial(\rho u_i)}{\partial x_i} = 0 \tag{1}$$

Momentum equations

$$\frac{\partial(\rho u_i u_j)}{\partial x_j} = -\frac{\partial p}{\partial x_i} + \frac{\partial}{\partial x_j}\left[\rho\nu\left(\frac{\partial u_i}{\partial x_j} + \frac{\partial u_j}{\partial x_i}\right) - \rho\overline{u_i' u_j'}\right] \tag{2}$$

In the equations, $(-\rho\overline{u_i' u_j'})$ denotes Reynolds stresses, p, u_i, u_j, ρ, and ν, respectively, denotes mean static pressure, mean velocity, turbulent fluctuation, density, and kinematic viscosity.

Turbulence equations

"The $k-\omega$ turbulence models is made up of two transport equations that give the rate of change of the turbulence kinetic energy (k) and the specific dissipation rate (ω) as a function of the combination of transport by convection and diffusion and the rate of production and decay of k and ω. The standard $k-\omega$ model equations are given below" [17,18].

$$k: \rho\left(\frac{\partial k}{\partial t} + \frac{\partial(u_j k)}{\partial x_j}\right) = \rho\left(\tau_{ij}\frac{\partial u_i}{\partial x_j} - \beta^* k\omega\right) + \frac{\partial}{\partial x_j}\left[\left(\mu + \sigma_k\rho\frac{k}{\omega}\right)\frac{\partial k}{\partial x_j}\right] \tag{3}$$

$$\omega: \rho\left(\frac{\partial \omega}{\partial t} + \frac{\partial(u_j \omega)}{\partial x_j}\right) = \rho\left(\alpha\frac{\omega}{k}\tau_{ij}\frac{\partial u_i}{\partial x_j} - \beta\omega^2\right) + \sigma_d\frac{\rho}{\omega}\frac{\partial k}{\partial x_j}\frac{\partial \omega}{\partial x_j} + \frac{\partial}{\partial x_j}\left[\left(\mu + \sigma_\omega\rho\frac{k}{\omega}\right)\frac{\partial \omega}{\partial x_j}\right] \tag{4}$$

The Reynolds stress is computed with the Boussinesq equation as:

$$\tau_{ij} = \mu_t\left(\frac{\partial u_i}{\partial x_j} + \frac{\partial u_j}{\partial x_i}\right) - \frac{2}{3}\rho k\delta_{ij} \tag{5}$$

where $\beta^*, \sigma_k, \alpha, \beta, \sigma_d$, and σ_ω are constants described as closure coefficients, whose values are available in Wilcox [18].

Pressure-based simulations were conducted under steady-state conditions using an absolute velocity formulation. The fluid domain was filled with air, considered as an incompressible ideal gas. Boundary conditions were established

following the guidelines outlined in Figure 4, with the no-slip wall condition implemented at the concentrator. A simple scheme was employed for pressure coupling, utilizing second-order spatial discretization for the pressure, momentum, and energy equations. All other conditions were maintained at their default values, and the standard initialization technique was utilized.

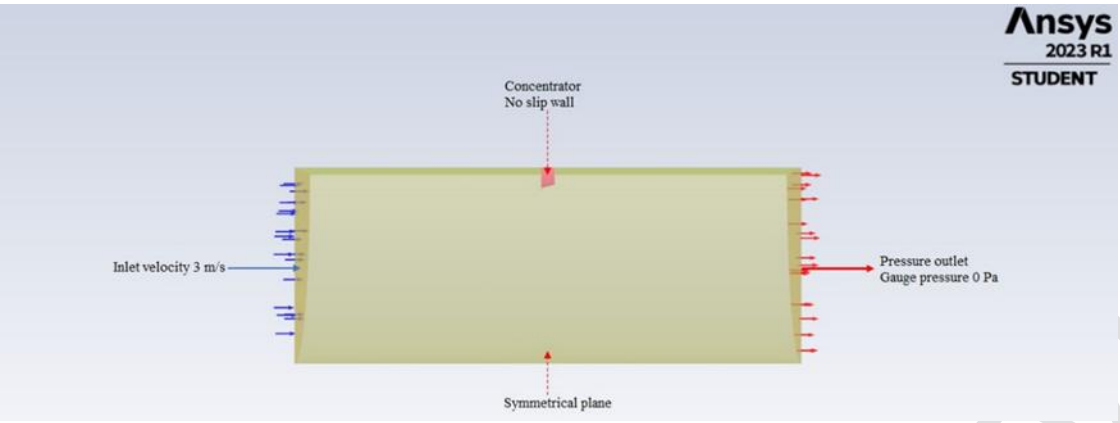

Figure 4. The boundary conditions

2.1.1 Determination of concentrator ratios

To investigate the effect of concentrator geometry on the performance of the concentrator, 45 concentrators were tested. The performance of the concentrator whose geometry is shown in Figure 1, was determined using dimensionless parameters in terms of concentrator efficiency (η_c) and velocity augmentation ratio (v_r). The concentrator length (L) to concentrator outlet diameter (D_o) ratio (L_r) and the difference between inlet and outlet radii (R_d) to D_o ratio (R_r) were used. For making the concentrator six equally spaced L_r were chosen between $L_r = 0.1$ and 0.6 inclusively. Thirteen equally spaced R_r were used between $R_r = 0.025$ and 0.325 inclusively. The concentrators are shown in Table 2 in terms of R_r and L_r.

Table 2. The R_r ranges for the tested concentrators for each L_r

R_r \ L_r	0.1	0.2	0.3	0.4	0.5	0.6
0.025	*	*	*	*	*	*
0.05	*	*	*	*	*	*
0.075		*	*	*	*	*
0.1		*	*	*	*	*
0.125			*	*	*	*
0.15			*	*	*	*
0.175				*	*	*
0.2				*	*	*
0.225				*	*	*

0.25	*	*
0.275	*	*
0.3		*
0.325		*

The concentrator outlet velocity (v_o), maximum velocity and position of maximum velocity were determined using velocity contours in Fluent. Using v_o and inlet velocity (v_i), the simulation velocity augmentation ratio ($v_{r,s}$) was calculated and analysed in in MATLAB using equation (6). For each value of L_r, a curve of v_r against R_r was plotted on the same graph for all values of L_r using MATLAB. This graph was used to determine an optimum L_r by taking the curve with highest values of $v_{r,s}$ at most points. A graph of $v_{r,s}$ against R_r was plotted for the optimum L_r. Optimum R_r was obtained at the maximum turning point of the curve.

$$v_{r,s} = \frac{v_o}{v_i} \tag{6}$$

2.1.2 Concentrator efficiency

The concentrator simulation efficiency ($\eta_{c,s}$) was determined using equation (7). A graph of $\eta_{c,s}$ against R_r for the optimum L_r was plotted. The equation of the curve was obtained using the curve fitting tool in MATLAB. The optimum concentrator efficiency ($\eta_{c,s,opt}$) was calculated using the curve equation for optimum R_r.

$$\eta_{c,s} = \frac{(p_i - p_o)_{ac}}{(0.5\rho)/(v_o^2 - v_i^2)} \tag{7}$$

where $(p_i - p_o)_{ac}$ denotes the actual pressure drop and $(0.5\rho_a)/(v_o^2 - v_i^2)$ is the ideal pressure drop across the concentrator.

2.1.3 The air dynamics

Using the optimum L_r and R_r one concentrator was created and used for analysing the air dynamics within the concentrator in Fluent. The following flow characteristics were analysed in CFD Post: pressure gradient, velocity gradient and turbulence intensity.

2.2 Validation of results

The computational analysis results were validated by lab-scale experiments. The concentrators were made with similar dimensions to the computational concentrators. A Pineware 40 cm Pedestal Fan (PPF4) with three plastic blades encased in removable grille was used to generate the wind. A 1.5 m long and 0.5 m diameter plastic cylinder, filled with small plastic pipes of 3 cm diameter was used to convert the from the fan to almost linear motion before it gets to the concentrator. The velocity and pressure were measured at the concentrator inlet and outlet using a PCE-007 anemometer and PTB110 barometer respectively. The data was recorded in respective data loggers at 30 s intervals for 30 minutes. The results were used to determine experimental velocity augmentation ratio ($v_{r,e}$) and concentrator efficiency ($\eta_{c,e}$). The results were compared with the computational analysis results. Uncertainity in simulation results was determined to establish the validity of the computational model.

3. RESULTS AND DISCUSSION

3.1 . Computational analysis results

Figure 5 shows the variation of $v_{r,s}$ with R_r. The $v_{r,s}$ changed with the change in both L_r and R_r. As L_r was increased from $L_r = 0.1$, the $v_{r,s}$ increased to a peak at $L_r = 0.4$ and then started to decrease. With reference to Figure 5, the velocity augmentation capability of short concentrators is low as shown by $v_{r,s}$ of 0.1096 and 1.1 for $L_r = 0.1$ and was between

1.128 and 1.184 for $L_r = 0.2$. It was also clear that the $v_{r,s}$ curves for $L_r = 0.5$ and 0.6 were lower than that the curves for $L_r = 0.3$ and 0.4.

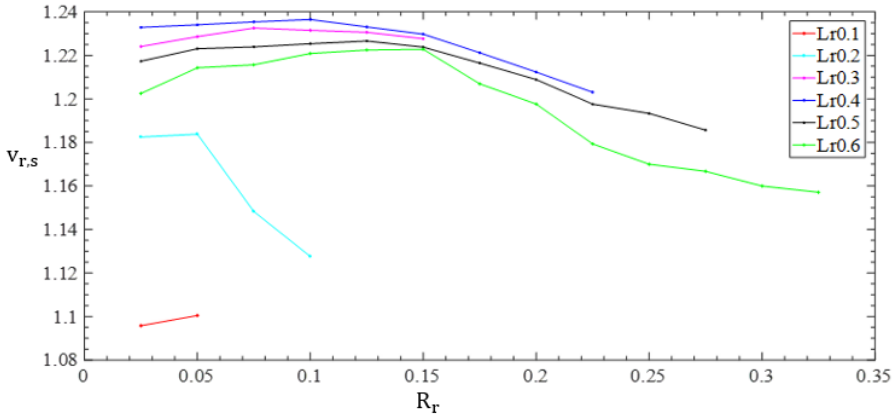

Fig 5. Concentrator velocity augmentation for different L_r against R_r

For the observed L_r range, the $v_{r,s}$ was low for low R_r; it increased to a peak at optimum R_r and then decreased as R_r was increased. Table shows the $v_{r,s}$ values at the beginning of the L_r range, at optimum R_r and at the end of the L_r. For $L_r = 0.3$, the $v_{r,s}$ at $R_r = 0.1$ was greater than the $v_{r,s}$ at the end of the L_r range.

Table 3. The $v_{r,s}$ values at the beginning of L_r range, at optimum R_r and the end of L_r range

L_r	$v_{r,s}$ at beginning of L_r range	Optimum R_r	Optimum $v_{r,s}$	$v_{r,s}$ at end of L_r range
0.1	1.096	0.05	1.1	1.1
0.2	1.182	0.05	1.184	1.128
0.3	1.229	0.075	1.235	1.228
0.4	1.233	0.1	1.236	1.203
0.5	1.217	0.125	1.227	1.186
0.6	1.202	0.15	1.223	1.157

Figure 6 shows the vortices that have been generated behind the flange. The vortices resulted in the formation of a low-pressure region behind the flange.

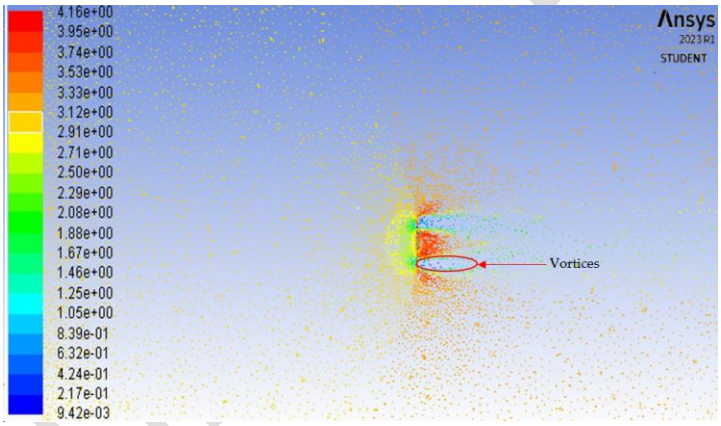

Fig 6. Vortices behind the flange

3.1.1 Effect of concentrator length to outlet diameter ratio (L_r) on velocity augmentation

Figure 7 to Figure 12 show velocity distribution along the concentrator for different L_r. All the concentrators have the same outlet radius ($r = 0.05$ m). A maximum speed of 3.77 m/s and 3.78 m/s was attained behind the concentrator outlet for $L_r = 0.1$ and 0.2 as shown in Figure 7 and 8 respectively.

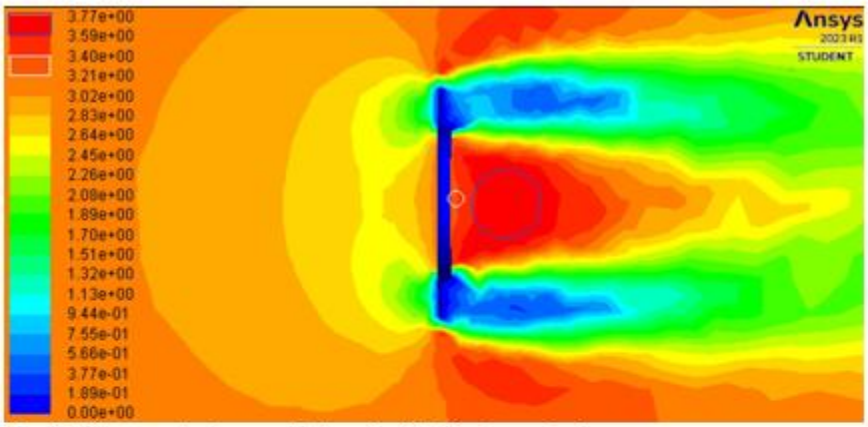

Fig 7. Concentrator outlet velocity for $L_r = 0.1$

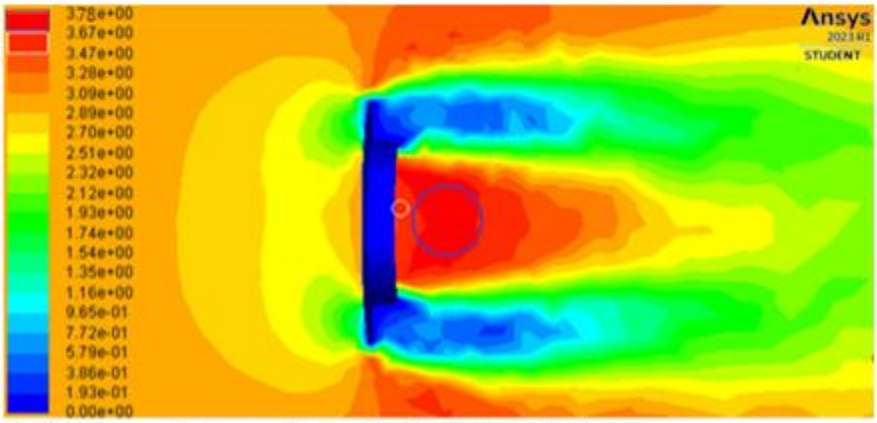

Fig 8. Concentrator outlet velocity for $L_r = 0.2$

As the concentrator length was increased, maximum velocity was attained at the concentrator outlet as shown from Figure 9 to Figure 12. The maximum velocity of 3.82 m/s was achieved at $L_r = 0.4$. For $L_r > 0.4$, smaller values of maximum velocity were observed (Figure 11 and 12) for all R_r.

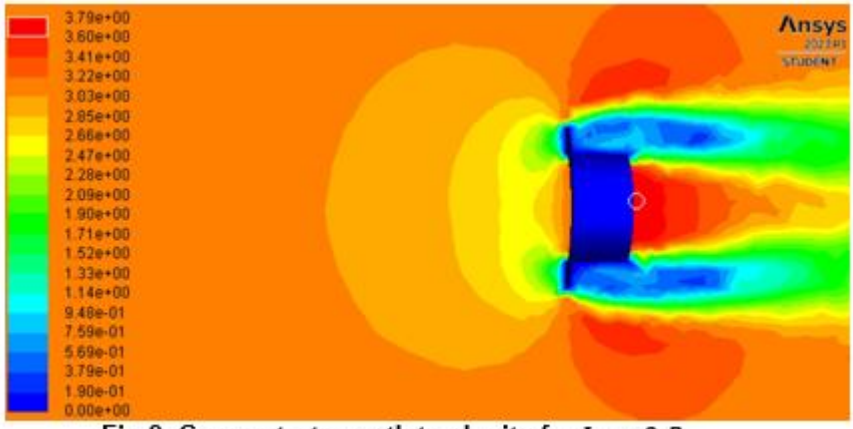

Fig 9. Concentrator outlet velocity for $L_r = 0.3$

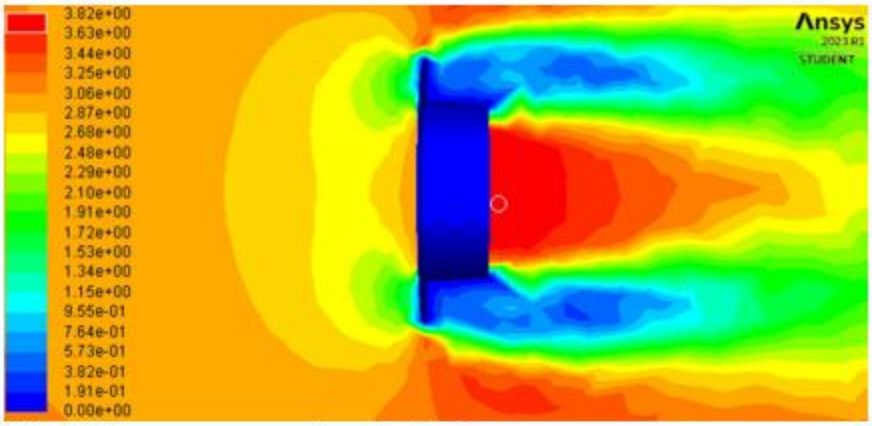

Fig 10. Concentrator outlet velocity for $L_r = 0.4$

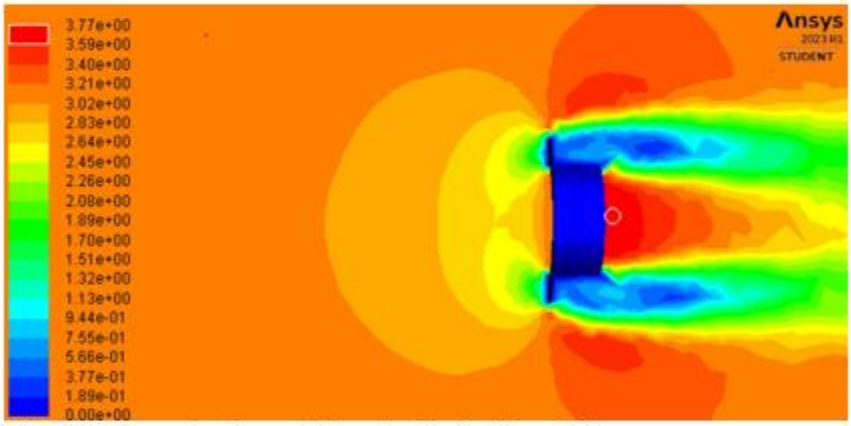

Fig 11. Concentrator outlet velocity for $L_r = 0.5$

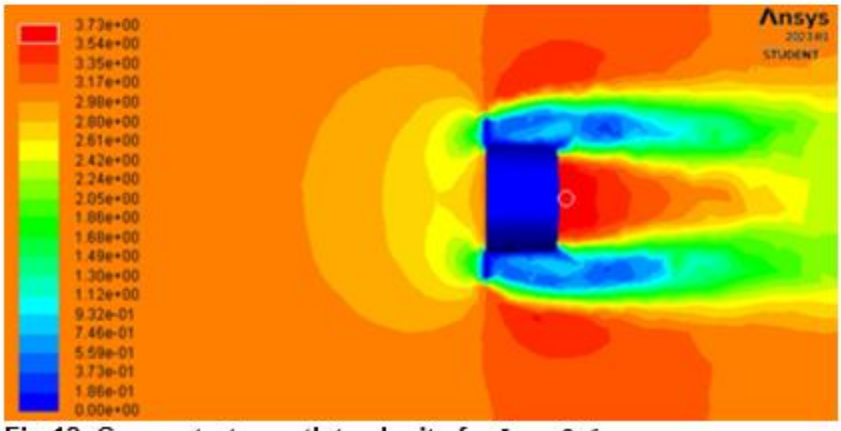

Fig 12. Concentrator outlet velocity for $L_r = 0.6$

3.1.2 The effect of the difference between concentrator inlet and outlet radius to outlet diameter ratio (R_r) on concentrator velocity augmentation

Figure 13 shows the variation of velocity augmentation ratio with R_r for $L_r = 0.4$. It is shown that $v_{r,s}$ increased from a minimum of 1.233 at $R_r = 0.0125$ to a maximum of 1.234 at $R_r = 0.1$ and decreased thereafter.

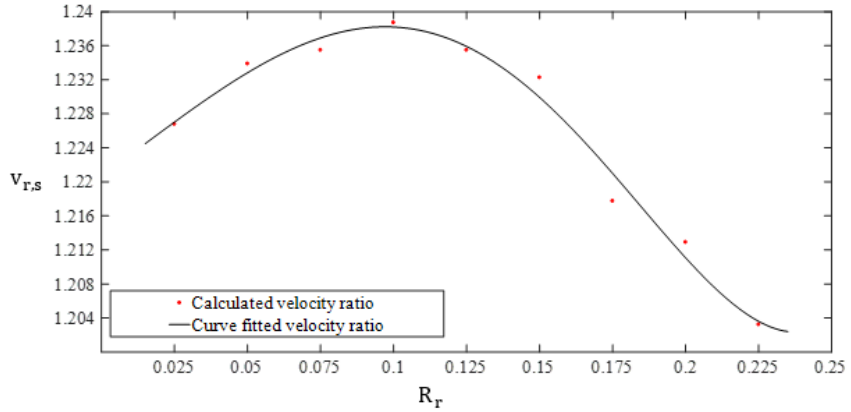

Fig 13. Variation of velocity augmentation with R_r for $L_r = 0.4$

Figure 13 also shows that when R was increased by increasing R_r, the percentage rate of velocity augmentation increase $|dv_{r,s}/dr|_{inc}$ was less than the percentage rate of velocity augmentation decrease $|dv_{r,s}/dr|_{dec}$ that is $|dv_{r,s}/dr|_{inc} < |dv_{r,s}/dr|_{dec}$. For example, an increase from $R_r = 0.025$ to 0.05 resulted in percentage $|dv_{r,s}/dr|_{inc} = 4.614\%$ while an increase from $R_r = 0.1$ to 0.125 resulted in $|dv_{r,s}/dr|_{inc} = 13.447\%$.

3.1.3 Concentrator efficiency

Figure 14 shows the variation of the simulation concentrator efficiency ($\eta_{c,s}$) with R_r The efficiency reduced with increasing R_r because as R_r was increased, the angle of incidence increased. Equation (8) expresses the concentrator efficiency obtained using the MATLAB curve fitting tool. The efficiency at optimum concentrator parameters $L_r = 0.4$ and $R_r = 0.1$ denoted by $\eta_{c,s,opt}$ was calculated using equation (8) and was equal to 0.8517

$$\eta_{c,s} = -1.949R_r^{0.3115} + 1.803 \quad (8)$$

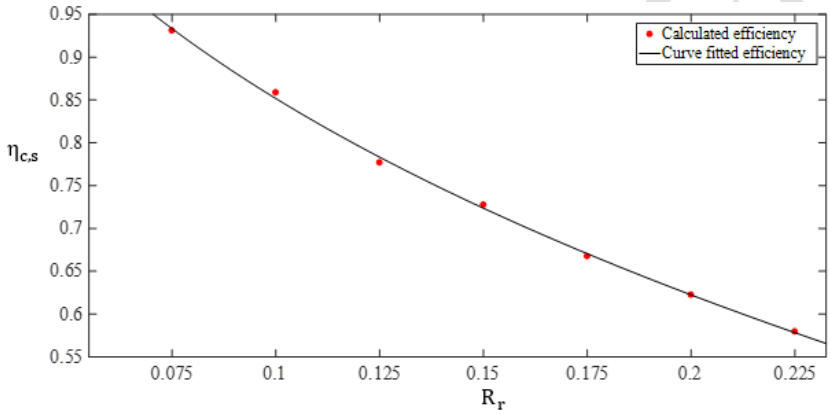

Fig 14. Variation of simulation concentrator efficiency with R_r for $L_r = 0.4$

3.1.4 The air dynamics

Figure 15. shows the variation of wind velocity with position along the x-axis at the positions between $2.75L$ before the concentrator inlet and $0.75L$ after the concentrator outlet. The wind decelerated as it approached the concentrator. From a distance L before the inlet, the wind accelerated constantly to a maximum speed at the concentrator outlet. It continued with this speed up to $0.5L$ distance behind the concentrator and started to decelerate.

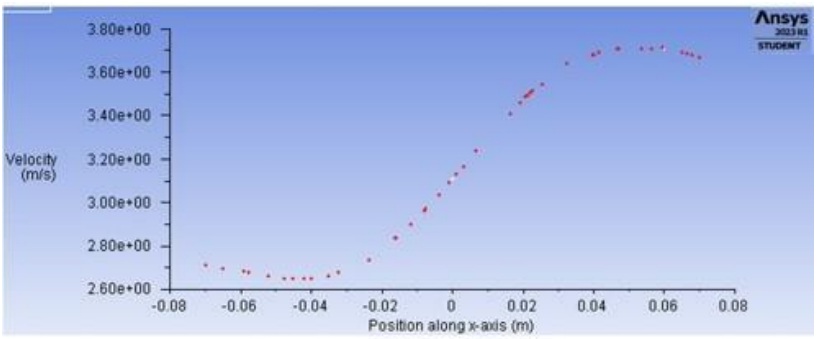

Fig 15. Variation of wind velocity with position in the horizontal direction

Figure 16. shows the variation of wind velocity with radial position at the concentrator outlet. The velocity was maximum from the concentrator centre to 80% of the outlet radius. It decreased to 0 m/s on the concentrator wall. At any distance greater than $0.1r$, the wind velocity was higher than the concentrator inlet velocity.

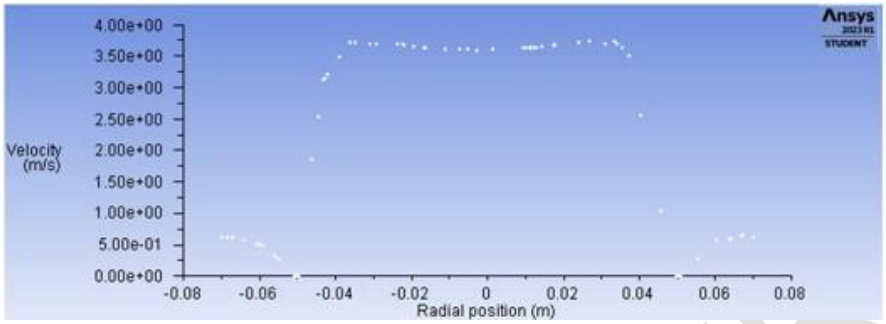

Fig 16. Variation of wind velocity with concentrator radial position

Pressure (P) is defined as force (F) per unit area (A) by the equation $P = F/A$, but this was violated in concentrators. Figure 17 shows that pressure decreased as the wind moved along the decreasing area of the concentrator.

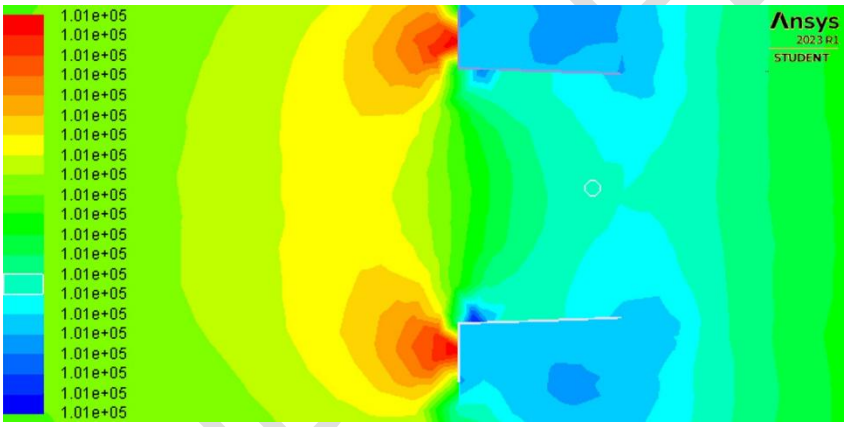

Fig 17. Reduction in air pressure as the concentrator area decreases

Figure 18 clearly shows that turbulence was very low in the concentrator. The turbulent intensity was around 1.85% for the greater part of the concentrator (except near the walls). It was relatively high behind the flange (21.67%).

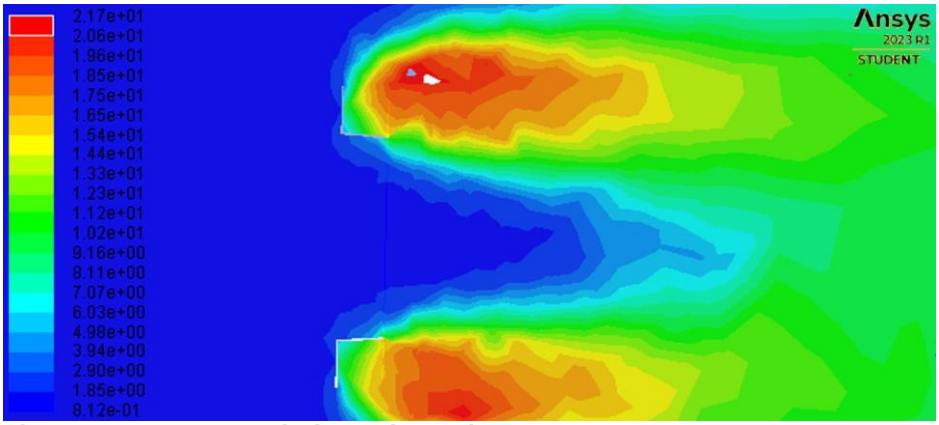

Fig 18. Percentage turbulence intensity

3.2 Validation of simulation results using experimental results

Figure 19 shows a comparison of the $v_{r,s}$ with $v_{r,e}$. Both curves show a similar pattern for the calculated v_r. Maximum velocity augmentation ratio was attained at $R_r = 0.1$ for both cases.

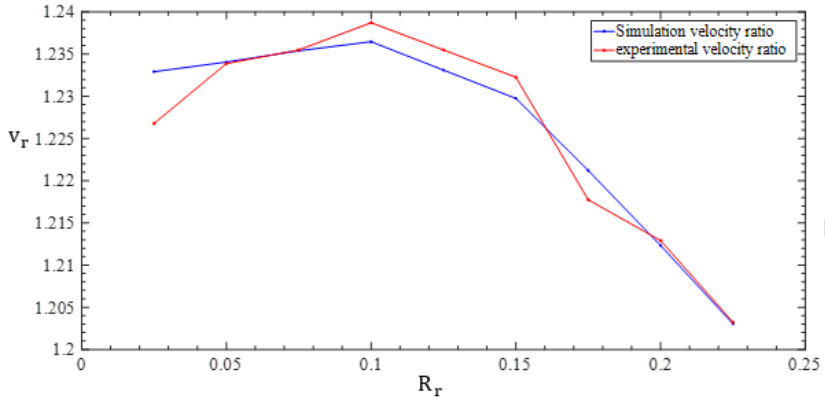

Fig 19. Comparison of variation of simulation and experimental velocity ratio with R_r for $L_r = 0.4$

The uncertainty in simulation velocity ratio (Uv_r) for $0.025 \leq R_r \leq 0.225$ was found to be in the range $-0.0061 \leq Uv_r \leq 0.0006$, which is very low, hence the simulation results are valid as they are very close to the experimental values. The average uncertainty in velocity was $Uv_r = 0.0002$.

Figure 20 compares the $\eta_{c,s}$ with the experimental concentrator efficiency ($\eta_{c,e}$). In both cases the efficiency decreases with increasing R_r.

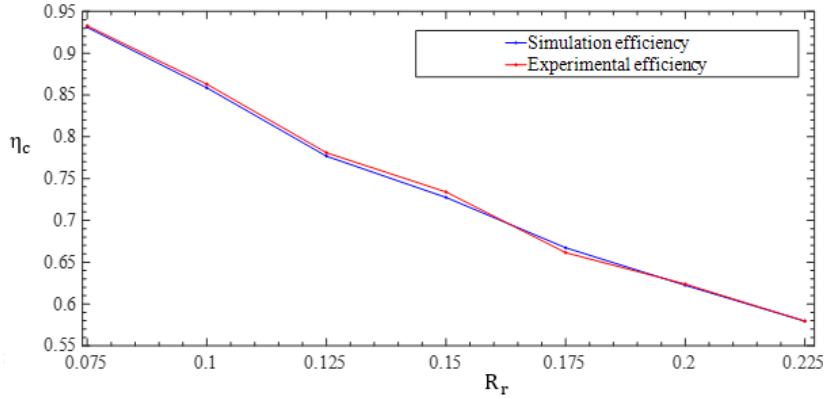

Fig 20. Comparison of variation of simulation and experimental concentrator efficiency with R_r for $L_r = 0.4$

The uncertainty in simulation efficiency (($U\eta$) was between -0.0059 and 0.0065 with average of 0.0018. The low $U\eta$ values imply that the simulation efficiency was very close to the measured efficiency, therefore the simulation was valid.

3.3 Discussion

"The angle θ_c influenced the angle of incidence of wind on the wall surface, which determined the amplification of wind velocity" [13]. "For short concentrators (low L), the friction on the walls occurred on a small range such that the energy losses due to friction were insignificant. However, the angle of incidence was large resulting in reduced component of wind velocity parallel to the concentrator wall. Thus, as the wind entered the concentrator more of it bombarded on the concentrator wall and lost kinetic energy resulting in deceleration which caused a decrease in velocity augmentation. Since wind had moved a relatively small distance, it continued to accelerate after the outlet and attained the maximum speed behind the concentrator outlet". [13]

As L was increased by increasing L_r, the incidence angle decreased resulting in an increased component of wind velocity parallel to the wall. Thus, energy loss due to wind bombarding on the concentrator wall was insignificant. However, the frictional losses occurred on an increased range. Therefore, too short, or too long concentrators are not good for wind velocity amplification. Thus, length optimisation is necessary to minimise energy losses. The findings here agree with results obtained by Mohanan et al. who found $v_r = 1.12$ for concentrators for L_r above 1 [1]. They suggested that concentrators should not be utilised as a duct for wind turbines. This study found out that medium sized concentrators are viable. There is need to carry out techno-economic analysis to check if they can be implemented.

If L is held as for concentrators whose velocity augmentation ratio is shown in Figure 13, the energy losses due to friction were constant and hence, the decrease in $v_{r,s}$ beyond $R_r = 0.1$ is due to increased energy losses due to decreased component of wind velocity parallel to the concentrator wall because of high incidence angle. The wind which was not parallel to the concentrator wall lost part of its kinetic energy as it bombarded on the concentrator wall surface. Hence, less energy was used on acceleration resulting in reduction in velocity augmentation.

"As the air flowed from the concentrator inlet along a decreasing cross-sectional area, the amount of the fluid passing through each point in time remained constant in accordance with the mass conservation principle" [19]. "Hence, to maintain the constant amount of airflow along the area gradient, the wind velocity at the concentrator outlet had to increase. Therefore, the concentrator outlet velocity was greater than the inlet for all concentrators irrespective of the R_r and the L_r". [19]

"As the air met the solid boundary of the concentrator, a shear stress which opposed the air flow was developed at the surface of contact and led to the dissipation of wind energy as the wind flowed through the concentrator" [20]. "There was additional resistance to air flow because of the non-uniformity of the velocity distribution across any section of the concentrator. The energy losses resulted in reduction in concentrator efficiency". [20]

The change in pressure along the area gradient occurred in accordance with the energy conservation principle and it provided the energy for accelerating the air mass along the concentrator. The air mass has potential, kinetic and pressure energy. Pressure energy causes random motion of the particles. It is this pressure energy that was converted to kinetic energy thus increasing the wind speed causing the pressure drop. Thus, the pressure at the outlet was lower than that at the inlet.

"The relatively high turbulent intensity behind the flange had an advantage of forcing wind to divert into the concentrator and increased the air mass flow rate. Turbulence is a well-known drawback for small wind turbines operation" [21]. "It increases stress and strain on the wind turbine and tower, which results in higher maintenance frequency for the generator and reduces the generator life span. Thus, the ability of concentrator in reducing turbulence makes them ideal for the small wind turbine industry. Low turbulence intensity in the concentrator plays a vital role in making a concentrator augmented wind turbine (CAWT) system produce electricity of relatively medium stability". [21]

In environments with high turbulence and directionally unstable wind vertical axis wind turbines have higher efficiency and produce more energy than HAWTs [22]. The low turbulence in the concentrator would enhance the efficiency and energy output of HAWTs such environments

The formation of vortices on the outside of the concentrator enhanced a pressure drop at the concentrator outlet, resulting in more mass flow through the concentrator [23,24]. Hence, a greater increase in the speed was achieved.

Previous research obtained optimum v_r = 9.8% at $L_r = 1.6$ (ref 1) and 23.3% for diffusers of same length, which led to the conclusion that CAWTs are not suitable for wind velocity augmentation. This agrees with the findings of this study , which showed a decrease in v_r for long concentrators from $L_r = 0.5$. However, this study found that medium length concentrators are good at velocity augmentation with optimum v_r = 23.6% at $L_r = 0.4$.

4. CONCLUSION

In conclusion, this study focused on optimizing the geometrical parameters of an empty concentrator-augmented wind turbine (CAWT). Through computational fluid dynamics (CFD) simulations and experimental validation, the study investigated the impact of the concentrator length to outlet diameter ratio (L_r) and the difference between the inlet and outlet radii to the outlet diameter ratio (R_r) on the concentrator's performance. The findings indicate that medium-length concentrators with an optimal L_r of 0.4 provide significant wind velocity augmentation, achieving a maximum velocity increment of 23.6%. Short concentrators showed limited velocity augmentation, while longer concentrators experienced a decrease in velocity augmentation beyond a certain point. The study emphasizes the importance of optimizing concentrator length to minimize energy losses and enhance wind turbine efficiency. Additionally, the air continued moving with this velocity up to 0.5L distance behind the concentrator and started to decelerate. Thus, it was concluded that when constructing a CAWT, the turbine rotor should be placed at any distance between the concentrator outlet and 0.5L behind the concentrator. It was shown that the wind velocity at the concentrator outlet at any radial distance greater than 0.1r from the concentrator wall was higher than the concentrator inlet velocity. Therefore, the blade tips of the turbine in a CAWT system should be at least 10% smaller than the concentrator outlet radius, for the whole rotor to receive wind with augmented velocity.

From the analysis, it was observed that the energy losses due to less air flowing parallel to the concentrator wall as a result of an increase in θ_c increased rapidly, causing a decrease in velocity augmentation beyond the optimum R_r at constant L_r. Therefore, modification of R_r beyond the optimum value is not effective for all L_r. It was also shown that the energy losses due to friction have a more negative impact on velocity augmentation than energy losses due to a large θ_c at high L_r.

The CFD analysis revealed the air dynamics within the concentrator, showing how velocity, pressure, and turbulence vary along the concentrator geometry. The low turbulence intensity in the concentrator makes it suitable for small wind turbine applications, where high turbulence can impact efficiency and maintenance. The experimental results validated the simulation outcomes, confirming the accuracy of the CFD model. The study contributes valuable insights into the design and optimization of concentrators for CAWT systems, highlighting the potential for medium-length concentrators to enhance wind energy production in areas with low wind speeds. Further techno-economic analysis is recommended to assess the feasibility of implementing these concentrators in practical wind energy systems.

ACRONYMS

CAWT	CONCENTRATOR AUGMENTED WIND TURBINE
DAWTS	DIFFUSER AUGMENTED WIND TURBINES
HAWTS	HORIZONTAL AXIS WIND TURBINES
RANS	REYNOLDS-AVERAGED NAVIER-STOKES

ABBREVIATIONS

CFD	COMPUTATIONAL FLUID DYNAMICS
RE	RENEWABLE ENERGY

NOMENCLATURE

L_r	CONCENTRATOR LENGTH TO OUTLET DIAMETER RATIO
p	MEAN STATIC PRESSURE
u_i'	MEAN VELOCITY
u_j'	TURBULENT FLUCTUATION
ρ	DENSITY
ν	KINEMATIC VISCOSITY
k	RATE OF CHANGE OF THE TURBULENCE KINETIC ENERGY
ω	SPECIFIC DISSIPATION RATE
$\beta^*, \sigma_k, \alpha, \beta, \sigma_d, \sigma_\omega$	CLOSURE COEFFICIENTS
η_c	CONCENTRATOR EFFICIENCY
v_r	VELOCITY AUGMENTATION RATIO
L	CONCENTRATOR LENGTH
D_o	CONCENTRATOR OUTLET DIAMETER
R_d	DIFFERENCE BETWEEN INLET AND OUTLET RADII
R_r	R_d TO D_o RATIO
v_o	CONCENTRATOR OUTLET VELOCITY
v_i	CONCENTRATOR INLET VELOCITY
$v_{r,s}$	SIMULATION VELOCITY AUGMENTATION RATIO
$\eta_{c,s}$	CONCENTRATOR SIMULATION EFFICIENCY
p_i	CONCENTRATOR INLET PRESSURE

p_o	**CONCENTRATOR OUTLET PRESSURE**
$v_{r,e}$	**EXPERIMENTAL VELOCITY AUGMENTATION RATIO**
$\eta_{c,e}$	**CONCENTRATOR EXPERIMENTAL EFFICIENCY**
Uv_r	**UNCERTAINTY IN SIMULATION VELOCITY RATIO**
$U\eta$	**UNCERTAINTY IN SIMULATION EFFICIENCY**

REFERENCES

1. Mohanan JN, Sundaramoorthy K, Sankaran A. Performance Improvement of a Low-Power Wind Turbine Using Conical Sections. Energies. 2021; 14.
2. Shambira N, Makaka G, Mukumba, P. Analytical Models for Concentrator and Diffuser Augmented Wind Turbines: A Review. Int. J. Smart Grid Clean Energy. 2021; 10:123–132.
3. Cloete S. The fundamental limitations of renewable energy. Accessed Jun 21, 2023. Available: http://www.theenergycollective.com/schalk-cloete/257351/fundamental-limitations-renewable-energy.
4. Khahro SF, Soomro AM, Tabbassum K, Dong L, Liao X. Assessment of Wind Power Potential at Hawksbay, Karachi Sindh, Pakistan. TELKOMNIKA. 2013; 11: 3479 -3490.
5. Dick E. Momentum Analysis of Wind Energy Concentrator Systems. Energy Convers Manag. 1984; 24(1):19–25.
6. Sedaghat A, Waked RA, Assad MEH, Khanafer K, Salim MNB. Analysis of Accelerating Devices for Enclosure Wind Turbines. Int J Astronaut Aeronautical Eng. 2017; 2:009.
7. Bukala J, Damaziak K, Kroszczynski K, Malachowski J, Szafranski T, Tomaszewski M et al. Small Wind Turbines: Specification, Design, and Economic Evaluation. In: Aissaoui AG, Tahour A., editors. Wind Turbines - Design, Control and Applications. Intech; 2016.
8. Shives M, Crawford C. Developing an Empirical Model for Ducted Tidal Turbine Performance Using Numerical Simulation Results In: Proc. IMechE Part A: J. Power and Energy. 2011; 226:112–125.
9. van Bussel GJW. The Science of Making More Torque from Wind: Diffuser Experiments and Theory Revisited. J Phys Conf Ser. 2007; 75: 012010.
10. Politis GK, Koras AD. A Performance Prediction Method for Ducted Medium Loaded Horizontal Axis Wind Turbines. Wind Engineering. 1995; 19: 272–288.
11. Vries Od. Fluid dynamic aspects of wind energy conversion. National Aerospace Laboratory NLR: London; 1979.
12. Aravindhan N, Bibin C, Ashok Kumar R, Sai Kalyan K, Sai Balaji K., Kugan R et al. S. Performance Analysis of Various Types of Ducted Wind Turbines – A Review. Mater Today Proc. 2023; 80: 188–194.
13. Shikha, S.; Bhatti, T.S.; Kothari, D.P. Air Concentrating Nozzles: A Promising Option for Wind Turbines. Int J Energy Technolo Policy. 2005; *3*: 394–412.
14. Aldhufairi M, Muda MKH, Mustapha F, Ahmad KA, Yidris N. Design of Wind Nozzle for Nozzle Augmented Wind Turbine. J. Adv. Res. Fluid Mech. Therm. Sci. 2022; 95(1): 36–43.
15. Shonhiwa C, Makaka G. Concentrator Augmented Wind Turbines: A Review. Renew. Sustain. Energy Rev. 2016; 59: 1415–1418.
16. Thangavelu SK, Goh CY, Sia CV. Design and Flow Simulation of Concentrator Augmented Wind Turbine. IOP Conf Ser Mater Sci Eng. 2019; 501.
17. Ajayi OO, Unser L, Ojo JO. Implicit Rule for the Application of the 2-Parameters RANS Turbulence Models to Solve Flow Problems around Wind Turbine Rotor Profiles. Clean Eng Technol. 2023; 13.
18. Wilcox DC. Formulation of the K-ω Turbulence Model Revisited. AIAA Journal. 2008; 46: 2823–2838.
19. Toth A, Bobok E, editors. Basic Equations of Fluid Mechanics and Thermodynamics. In: Flow and Heat Transfer in Geothermal Systems. Elsevier; 2017.
20. Al-Quraishi BAJ, Asmuin NZB, Mohd S B, Abd Al-Wahid WA, Mohammed AN, Didane DH. Review on Diffuser Augmented Wind Turbine (DAWT). Int. J. of Integrated Engineering. 2019;11: 178–206.
21. Sagrillo M, Sagrillo P. Small Turbine Column: Siting Towers & Heights for Small Wind Turbines. WINDLETTER. 2005; 24: 1–2.
22. Das Karmakar S, Chattopadhyay H. A Review of Augmentation Methods to Enhance the Performance of Vertical Axis Wind Turbine. Sustain. Energy Technol. Assess. 2022: 53: 102469.
23. Ohya Y, Karasudani T. A Shrouded Wind Turbine Generating High Output Power with Wind-Lens Technology. Energies. 2010; 3: 634–649.
24. Ohya Y, Karasudani T, Sakurai A, Abe KI, Inoue M. Development of a Shrouded Wind Turbine with a Flanged Diffuser. J. Wind Eng. Ind. Aerodyn. 2008; 96: 524–539.